



HAL
open science

Asymptotic regimes in elastohydrodynamic and stochastic leveling on a viscous film

Christian Pedersen, John Niven, Thomas Salez, Kari Dalnoki-Veress, Andreas Carlson

► **To cite this version:**

Christian Pedersen, John Niven, Thomas Salez, Kari Dalnoki-Veress, Andreas Carlson. Asymptotic regimes in elastohydrodynamic and stochastic leveling on a viscous film. 2019. hal-02052718v1

HAL Id: hal-02052718

<https://hal.science/hal-02052718v1>

Preprint submitted on 28 Feb 2019 (v1), last revised 25 Sep 2019 (v2)

HAL is a multi-disciplinary open access archive for the deposit and dissemination of scientific research documents, whether they are published or not. The documents may come from teaching and research institutions in France or abroad, or from public or private research centers.

L'archive ouverte pluridisciplinaire **HAL**, est destinée au dépôt et à la diffusion de documents scientifiques de niveau recherche, publiés ou non, émanant des établissements d'enseignement et de recherche français ou étrangers, des laboratoires publics ou privés.

Asymptotic regimes in elastohydrodynamic and stochastic leveling on a viscous film

Christian Pedersen,¹ John Niven,² Thomas Salez,^{3,4} Kari Dalnoki-Veress,² and Andreas Carlson^{1,*}

¹*Mechanics Division, Department of Mathematics, University of Oslo, 0316 Oslo, Norway.*

²*Department of Physics and Astronomy, McMaster University,
1280 Main Street West, Hamilton, Ontario, L8S 4M1, Canada.*

³*Univ. Bordeaux, CNRS, LOMA, UMR 5798, F-33405 Talence, France.*

⁴*Global Station for Soft Matter, Global Institution for Collaborative Research and Education,
Hokkaido University, Sapporo, Hokkaido 060-0808, Japan.*

(Dated: February 27, 2019)

An interface of finite thickness that is elastic and deforms near a solid substrate in a viscous fluid is a situation relevant to various dynamical processes in biology, geophysics and engineering. Here, we study the relaxation dynamics of an elastic plate resting on a thin viscous film that is supported by a solid substrate. By combining scaling analysis, numerical simulations and experiments, we identify asymptotic regimes for the elastohydrodynamic leveling of a surface perturbation of the form of a bump, when the flow is driven by either the elastic bending of the plate or thermal fluctuations. In both cases, two distinct regimes are identified when the bump height is either much larger or much smaller than the thickness of the pre-wetted viscous film. Our analysis reveals a distinct crossover between the similarity exponents with the ratio of the perturbation height to the film height.

I. INTRODUCTION

The motion of an elastic sheet supported by a thin layer of viscous fluid is a phenomenon that manifests itself in processes spanning wide ranges of time and length scales, from *e.g.* magmatic intrusion in the Earth's crust [1, 2], to fracturing and crack formation in glaciers [3], to pumping in the digestive and arterial systems [4–6], or the construction of 2D crystals for electronic engineering [7]. Elastohydrodynamic flows have been studied in model geometries in order to understand their generic features and the inherent coupling between the driving force from the elastic deformations of the material and the viscous friction force resisting motion [8–18]. For instance, when an elastic sheet deforms onto a wall pre-wetted by a thin viscous film, the dynamics of the advancing front is dictated by the local curvature of the interface [19]. This elastohydrodynamic relaxation is reminiscent of the capillary spreading of a viscous drop onto a solid substrate [20–23]. Similar to capillary flows, elastohydrodynamic relaxation processes are not only limited to very thin pre-wetted films. In fact, an elastic sheet with zero spontaneous curvature but with an initial shape of a bump (Fig. 1) with a height much larger than the pre-wetted viscous film will relax towards a flat equilibrium state. Inevitably, the system must then crossover from a situation where the bump height is larger than the pre-wetted film height, to a situation where instead the pre-wetted film becomes thicker than the bump. We are wondering how the elastohydrodynamic leveling changes with the ratio between the bump height and the pre-wetted film thickness. In particular, are there different asymptotic regimes, and how do we transition from one to another? At the nanoscale, thermal fluctuations are expected to contribute and may even dominate the dynamics [24–28], which we would like to quantify further in the leveling dynamics. To answer these questions, we combine numerical solutions of a mathematical model based on the lubrication theory [29] with scaling analysis and experiments.

II. MATHEMATICAL MODEL AND NUMERICAL PROCEEDURE

We consider the model system depicted in Fig. 1, where we focus on a system where gravity can be neglected, *i.e.*, the bump height is smaller than the elasto-gravity length [8]. Only situations where the height $\hat{h}(x, t)$ of the fluid film is small compared its horizontal extent and where the film slopes are small, *i.e.* $\partial h(x, t)/\partial x \ll 1$, are considered. We describe the viscous flow between the plate and the solid substrate through lubrication theory [29]. When the deflection of the elastic plate is small compared to its thickness d , we can neglect stretching and the pressure reduces to $p(x, t) = B\partial^4\hat{h}(x, t)/\partial x^4$, where $B = Ed^3/[12(1 - \nu^2)]$ is the bending rigidity of the plate, E is the Young modulus and ν is the Poisson ratio [30]. By assuming incompressible flow and imposing no-slip conditions at the two solid

* acarlson@math.uio.no

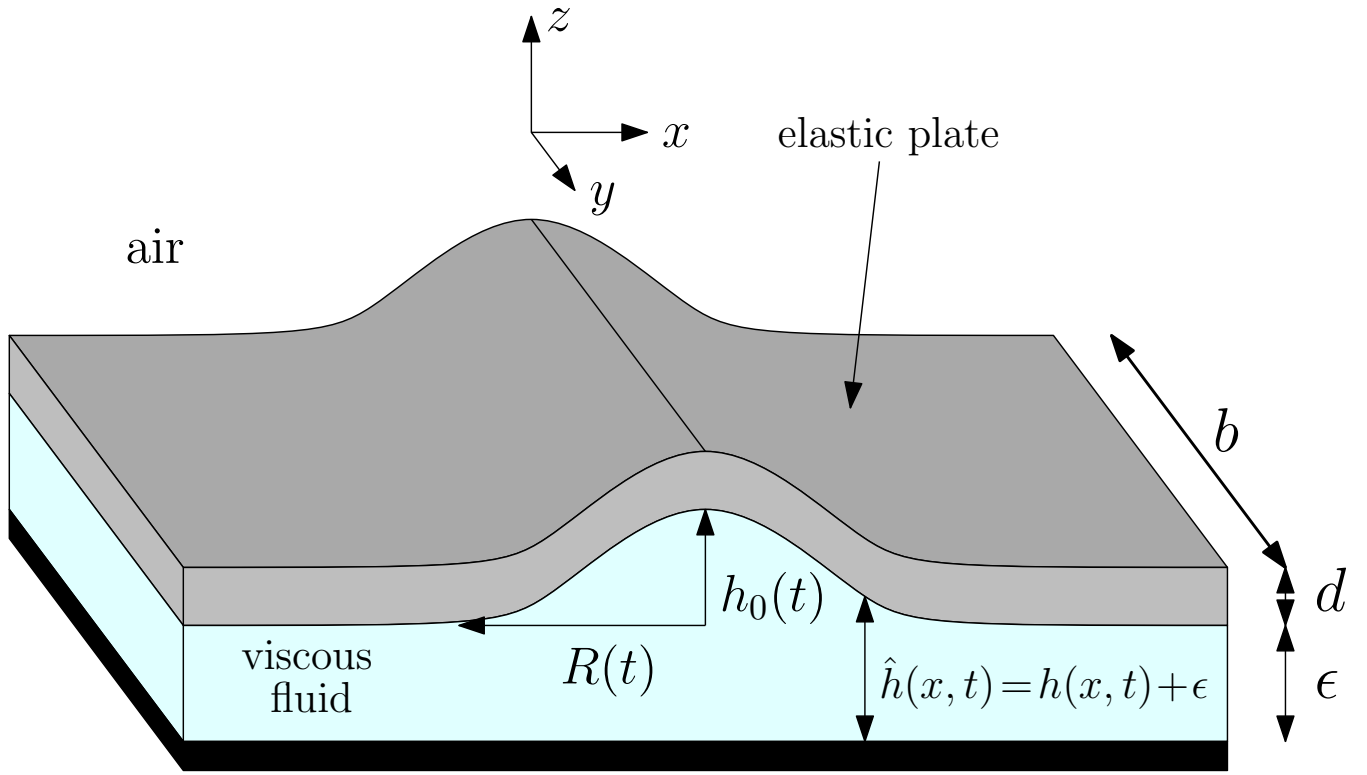


FIG. 1. Schematic of the system. An elastic plate is supported by a viscous film on a solid substrate, in air. The elastic plate has a thickness d and a width b . Initially, the overall profile presents a localized bump, whose profile is even in the x -direction and invariant in the y -direction. Far away from the perturbation, the viscous film has a constant thickness ϵ . In the bump region, the height profiles $\hat{h}(x, t)$ and $h(x, t) = \hat{h}(x, t) - \epsilon$ of the viscous film and the bump, respectively, vary with the horizontal position x and time t , and remain symmetric about $x = 0$. At $x = 0$, we define the characteristic height $h(x = 0, t) = h_0(t)$ of the bump and its typical radius $R(t)$, with initial values given as $h_0(t = 0) = h_i$ and $R(t = 0) = R_i$.

substrates, one obtains the governing equation for the evolution of the height profile (see *e.g.* Ref. [8]) and we consider a one-dimensional geometry as we assume no variations along the y -direction

$$\frac{\partial \hat{h}(x, t)}{\partial t} = \frac{\partial}{\partial x} \left[\frac{B}{12\mu} \hat{h}^3(x, t) \frac{\partial^5 \hat{h}(x, t)}{\partial x^5} + \Gamma \hat{h}^{3/2}(x, t) \eta(x, t) \right], \quad (1)$$

where μ is the fluid's dynamic viscosity. At small scales, thermal fluctuations can also influence the dynamics, which is described by the last term in Eq. (1), originating from an additional symmetric random stress term in the Navier-Stokes equations [31]. The amplitude of this term is $\Gamma = \sqrt{k_B T_A / (6\mu b)}$ where k_B is the Boltzmann constant and T_A is the ambient temperature, b is the width of the plate along the y -direction, and $\eta(x, t)$ is modelled as a spatiotemporal Gaussian white noise such that $\langle \eta(x, t) \rangle = 0$ and $\langle \eta(x, t) \eta(x', t') \rangle = \delta(x - x') \delta(t - t')$, where $\langle \rangle$ indicate average quantities. We non-dimensionalize Eq. (1) by: $X = x/R_i$, $\hat{H}(X, T) = \hat{h}(x, t)/h_i$, $T = t B h_i^3 / (12\mu R_i^6)$, and $\Theta(X, T) = \eta(x, t) \sqrt{12\mu R_i^7 / (B h_i^3)}$. When $\Gamma = 0$, this non-dimensionalization procedure gives us a parameter-free partial differential equation for $\hat{H}(X, T)$. When $\Gamma > 0$, the non-dimensional number $N = \sqrt{2k_B T_A R_i^3 / (B h_i^2 b)}$ appears as a pre-factor in front of the stochastic term, and N^2 measures the ratio between thermal and bending energies.

When we solve the dimensionless version of Eq. (1) numerically with the finite element method we split it into three coupled equations for: the bump profile $H(X, T) = \hat{H}(X, T) - \epsilon/h_i$, the linearized curvature $\partial^2 H(X, T) / \partial X^2$, and the bending pressure $\partial^4 H(X, T) / \partial X^4$. These fields are discretized with linear elements and solved by using Newton's method from the FEniCS library [32]. For the deterministic case $N = 0$, an adaptive time stepping routine has been used with an upper time step limit of $\Delta T = 0.001$ and a discretization in space $\Delta X \in [0.001; 0.01]$. For the stochastic case $N > 0$, we have used a constant time step $\Delta T = 0.001$, together with a discretization in space $\Delta X = 0.0025$. When $N = 0$, we impose the initial condition: $H(X, T = 0) = (1 - X^2)^2$ for $-1 \leq X \leq 1$ [19] and $H(X, T = 0) = 0$ otherwise. When $N > 0$, we impose the initial condition: $H(X, T = 0) = 1 - \tanh(50X^2)$ with a shorter horizontal

length scale in order to reduce the computational time and we checked that using this initial condition for $N = 0$ does not affect the results presented here. We further impose the following boundary conditions at the boundary $\partial\Omega$ of the numerical domain: $H(X \in \partial\Omega, T) = H(X \in \partial\Omega, 0)$, $\partial^2 H(X \in \partial\Omega, T)/\partial X^2 = 0$, and $\partial^4 H(X \in \partial\Omega, T)/\partial X^4 = 0$. The noise $\Theta(X, T)$ is implemented independently at each nodal point and time step using the "random" class from the Numpy library [33], with zero mean and unit variance.

III. EXPERIMENTAL PROCEDURE

The samples consist of a fiber of liquid polystyrene (PS) with a glass-transition temperature $T_{g, \text{PS}} \approx 100^\circ\text{C}$ deposited on a PS film supported on a silicon (Si) substrate. These samples are capped by a thin sheet of polysulfone (PSU) with $T_{g, \text{PSU}} \approx 180^\circ\text{C}$. The sample preparation is carried out as follows: PS fibers (with number-averaged molecular weight $M_n = 15.8$ kg/mol, and polydispersity index $\text{PDI} = 1.05$, Polymer Source Inc., Canada) are pulled from the melt at 175°C by using a glass rod. Thin PS films are spin cast from a toluene solution onto 10×10 mm² Si substrates, leading to a thickness of 25 to 380 nm that we measure by using ellipsometry (Accurion, EP3). The films are annealed at 110°C for at least 12 hours in vacuum to remove any residual solvent and to relax residual stresses. The PS fibers are then transferred onto the PS films and briefly heated above $T_{g, \text{PS}}$. The heating allows the PS to flow, thereby resulting in a bump. Thin PSU films ($M_n \approx 22$ kg/mol, Sigma-Aldrich) are prepared by spin casting from a cyclohexanone solution onto freshly cleaved mica substrates (Ted Pella, USA). The PSU films have a thickness of ≈ 160 nm, measured using ellipsometry, and are annealed in vacuum at 200°C for at least 12 hours. The PSU films are floated onto water and then transferred onto a supporting apparatus (details are found in Ref. [34]), held only by the film edges. These freestanding PSU films can be relaxed to an unstrained state ensuring no in-plane tension and in the last step transferred onto the PS sample.

After the above preparation, the samples are annealed on a hotstage (Linkam, UK) at 130°C , which is above $T_{g, \text{PS}}$ but below $T_{g, \text{PSU}}$. This makes the PS to become a viscous liquid while the capping PSU film remains an elastic solid, composing the effective two-dimensional setup described in Fig. 1. The height profile is imaged during annealing using optical microscopy with a red laser line filter ($\lambda = 632.8$ nm, Newport, USA), which creates interference fringes in the region of the bump, as shown in Fig. 2(a), due to the reflected light from the Si substrate. Each interference fringe corresponds to a change in height of $\lambda/(4n)$, where $n \approx 1.57$ is the average index of refraction of the two polymers that make up the sample ($n_{\text{PS}}=1.53$ and $n_{\text{PSU}}=1.61$). This allows the bump profile $h(x, t)$ to be reconstructed by fitting an even power polynomial to the fringe data, as shown in Fig. 2(b) and allows us to track the height dynamics shown in Fig. 2(c). Such profiles can then be used to track the leveling dynamics, and to extract in particular the evolution of the height $h_0(t)$ of the bump with time for various initial geometries.

IV. RESULTS

A. Elastohydrodynamic leveling

We first start by investigating the elastohydrodynamic leveling in the absence of thermal fluctuations ($N = 0$). In Fig. 3 we show the numerical solutions of the dimensionless version of Eq. (1) for $N = 0$ and we can see that the aspect ratio h_i/ϵ controls both the time scale for leveling and the detailed features of height profile. The smaller h_i/ϵ , the faster the dimensionless leveling process. Also, the dip created near the advancing front of the perturbation is enhanced both in magnitude and lateral extent for smaller h_i/ϵ . We remark that for each initial aspect ratio there is a transition period of a few numerical time steps preceding the onset of the leveling process. This period is not included in Fig. 4 as it is considered as an influence created by the initial condition, but does not influence the later dynamics. For $h_i/\epsilon = 43$, the numerical height profiles are further compared with our experiments, which are found to be in good agreement. We recall here that the elastic plate is floating on the liquid film and has edges that are free to move. Therefore, the pressure contribution from bending still largely dominates any contribution from stretching, where Eq. (1) is still valid.

We now turn to a scaling analysis of Eq. (1) for $N = 0$. When $h_0(t)/\epsilon \ll 1$, the equation can be linearized and reduces to $12\mu\partial h/\partial t = B\epsilon^3\partial^6 h/\partial x^6$ and we deduce the long-term scaling for the temporal evolution of the horizontal length of the bump: $R(t) \sim [B\epsilon^3 t/(12\mu)]^{1/6}$. Since there is area conservation in the (x, z) -plane, we assume $R(t)h_0(t)$ to be constant, that is evaluated to $R_i h_i$ at $t = 0$. By combining these scaling relations we get for $h_0(t)/\epsilon \ll 1$

$$\frac{h_0(t)}{\epsilon} \sim \left(\frac{\tau}{t}\right)^{1/6}, \quad (2)$$

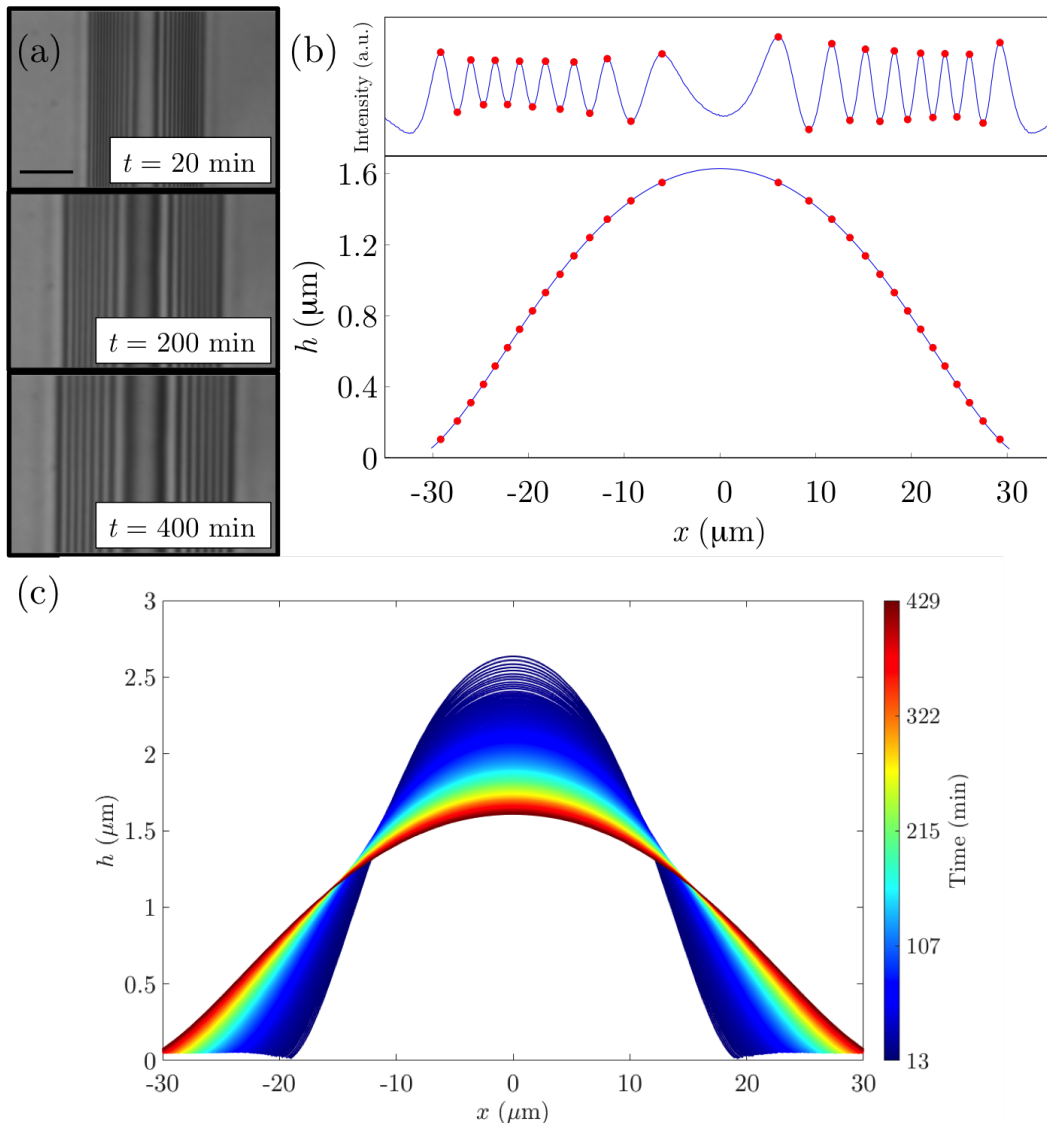


FIG. 2. (a) Typical optical microscopy images showing the temporal evolution of the interference fringes due to the liquid bump capped by the elastic plate ($20 \mu\text{m}$ scale bar). (b) Intensity profile averaged along the y -direction of the bump at a given time t , and corresponding reconstructed bump profile at 400 minutes. (c) Temporal evolution of the bump profile.

where $\tau = 12\mu h_i^6 R_i^6 / (B\epsilon^9)$ is the characteristic time scale for the bending-driven leveling dynamics. When $h_0(t)/\epsilon \gg 1$, we need to match the curvature of a traveling-wave solution localized near the advancing front with the quasi-static solution [19], *i.e.*, constant pressure p in the bump, leading to [27]

$$\frac{h_0(t)}{\epsilon} \sim \left(\frac{\tau}{t}\right)^{2/17}. \quad (3)$$

By balancing the two asymptotic predictions above, we expect the crossover between them to occur around $t/\tau \approx 1$. In addition, these asymptotic regimes suggest that $h_0(t)/\epsilon$ is essentially a function of t/τ only, independent of the value of h_i/ϵ in particular.

In order to test our scaling predictions, we compute numerical solutions of the dimensionless version of Eq. (1) for $N = 0$, with $h_i/\epsilon \in [10^{-2}, 10^3]$ and extract $h_0(t)/\epsilon$ as a function of t/τ . These numerical results are plotted in Fig. 4 and compared to the experimental data. For each sample, the experimental data is matched to the numerical data through one free fitting parameter α in front of the time scale τ . The values of the fluid viscosity and elastic Young modulus are highly sensitive to temperature in the experiments, and we estimate them to be $\mu \approx 10^4$ Pa.s [35, 36] and

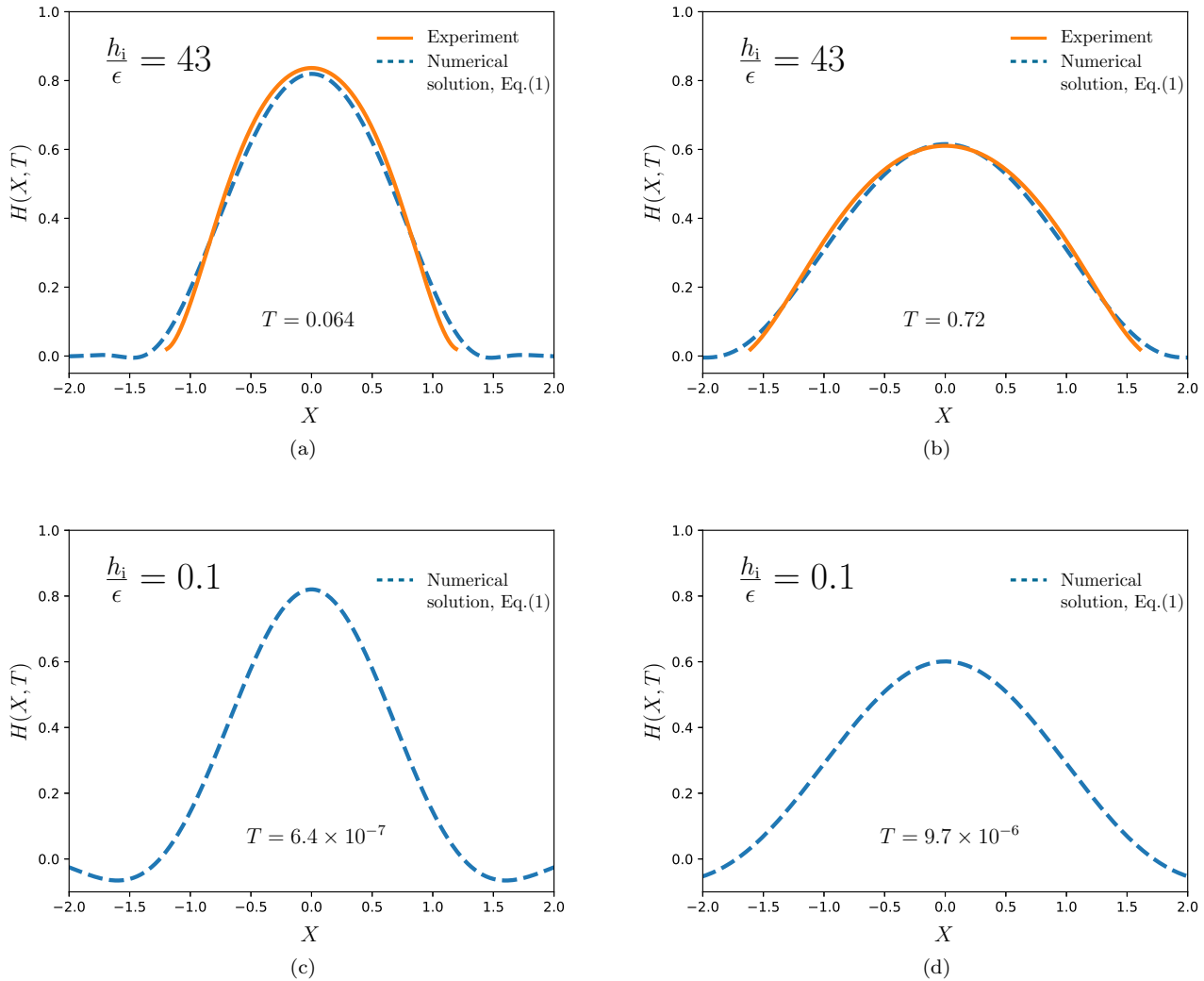


FIG. 3. (a-b) Bump height profiles for an initial aspect ratio $h_i/\epsilon = 43$, from a numerical solution and an experiment at two dimensionless times T as indicated, which correspond respectively to $t = 37$ min and $t = 416$ min. The geometrical parameters are $h_i = 2.9 \mu\text{m}$, $R_i = 16.5 \mu\text{m}$, and $\epsilon = 67$ nm. In order to account for the experimental uncertainties in the geometrical parameters, the experimental time t is divided by a free fitting factor $\alpha = 0.13$. Note that, specifically for these figures, the initial condition for the numerical solution was fixed by a curve fitting of the actual experimental profile at $t = 13$ min. (c-d) Bump height profiles for an initial aspect ratio $h_i/\epsilon = 0.1$, from a numerical solution at two dimensionless times T , as indicated, chosen so that the central heights $H(X = 0, T)$ match the ones in the top row.

$E \approx 2.6$ GPa [37], respectively. Since all experiments were carried out at the same temperature and with the same polymer, sample-to-sample variations in τ result only from uncertainties in the geometrical parameters h_i , R_i , d , and ϵ . The obtained α values are 0.13, 0.7, and 1.3 for the three samples and each of these values are reasonably close to unity. More importantly, the sample-to-sample variations in α do not exceed a factor of 10, which is well within the expected relative error arising from the high sensitivity of τ to the geometrical parameters. The general agreement between the experimental data and the numerical predictions is good, over about 5 orders of magnitude in t/τ . The systematic early-time tail in the experimental data might be attributed to the initial compressive thermal stresses in the elastic layer, which arise due to the rapid heating of the samples from room temperature to $T = 130^\circ\text{C}$, which relax prior to leveling and the time needed for the initial shape to enter the asymptotic regime [22, 38].

The master curve in Fig. 4 confirms that $h_0(t)/\epsilon$ is a function of t/τ . Furthermore, the two scaling regimes predicted above are indeed present, with pre-factors close to unity, and the crossover between the two being located near $t/\tau \approx 1$ as predicted. Any bump that initially starts in a thin pre-wetted film regime $h_0(t)/\epsilon \gg 1$ will eventually crossover to a thick-film regime $h_0(t)/\epsilon \ll 1$, with the corresponding power laws in time. As a final remark, a similar combination

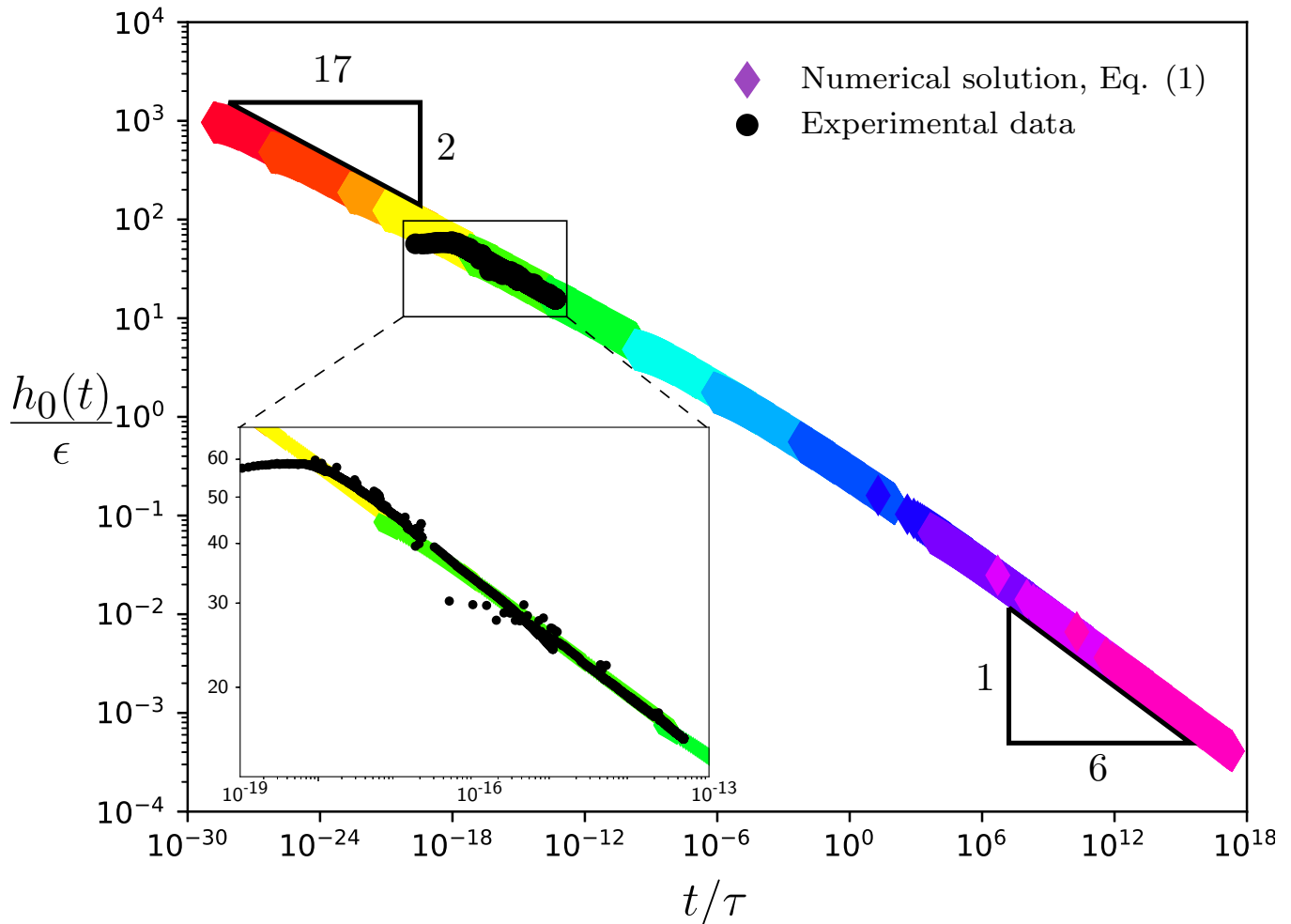


FIG. 4. Non-dimensional bump height as a function of dimensionless time in the bending case, for various initial values of $h_i/\epsilon \in [10^{-2}; 10^3]$. The coloured diamond-shaped markers are rescaled data points from the numerical solutions of the dimensionless version of Eq. (1) with $N = 0$, and the black circle-shaped markers are scaled experimental data points. The exponents of the two asymptotic regimes of Eqs. (2) and (3) are indicated with triangles. The inset provides a zoom in the region containing the experimental data for the three samples, with initial aspect ratios $h_i/\epsilon = 30, 43, 56$; corresponding respectively to $\epsilon = 50, 67, 26$ nm; $h_i = 1.52, 2.9, 1.48$ μm ; and $R_i = 9.6, 16.5, 9.9$ μm . The uncertainties in all experimental length scales are about 5%. To compensate for those, the characteristic time τ for each sample is multiplied by a free fitting factor $\alpha = 0.7, 0.13, 1.3$, respectively.

(not included here) of numerical simulations and scaling analysis can be performed for an axisymmetric geometry, leading to $h_0(t) \sim t^{-2/11}$ for $h_i/\epsilon \gg 1$, and $h_0(t) \sim t^{-1/3}$ for $h_i/\epsilon \ll 1$.

B. Stochastic leveling

We investigate here the leveling process when it is dominated by thermal fluctuations ($N > 0$). As shown in Fig. 5, the numerical solutions suggest that the aspect ratio h_i/ϵ is again essential, as it sets the time scale for leveling where the smaller h_i/ϵ , the faster the dimensionless leveling process. Moreover, by comparison with the deterministic ($N = 0$) case in Fig. 3, the stochastic ($N > 0$) profiles exhibit spatiotemporal fluctuations and adopt different average shapes and leveling dynamics.

To go further, we propose a scaling analysis of Eq. (1), inspired by Ref. [22]. We consider specifically the $N \gg 1$ limit, for which the thermal fluctuations are the dominant driving contribution to the dynamics and we assume that we can neglect the bending term so that Eq. (1) reduces to $\partial h/\partial t = \Gamma \partial[(\epsilon + h)^{3/2} \eta]/\partial x$. We consider the average quantities $\langle h_0(t) \rangle$ and $\langle R(t) \rangle$, where we invoke a $\sim (tx)^{-1/2}$ scaling [24] for the root mean square value of the averaged

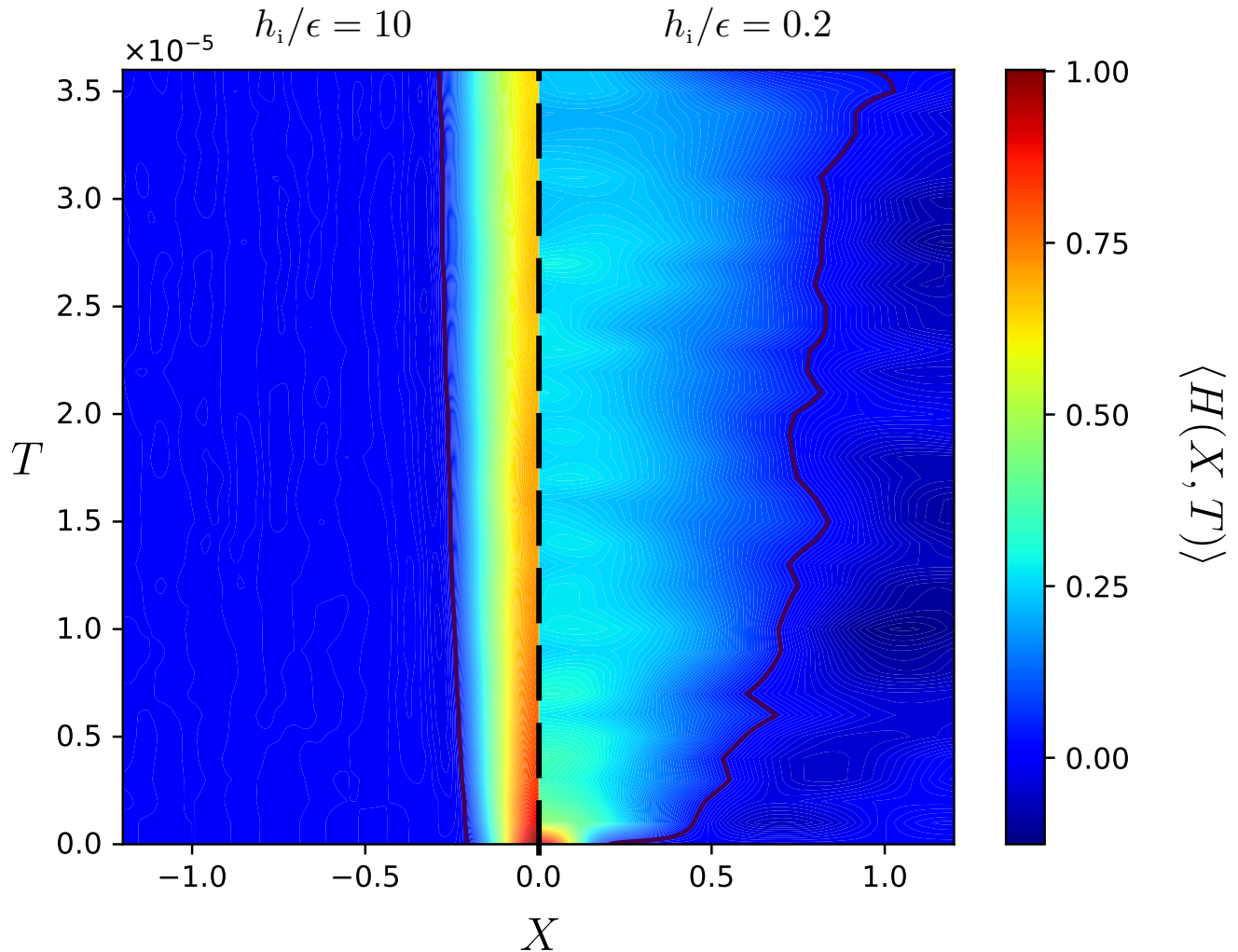


FIG. 5. Contour plot of the dimensionless bump height profile $\langle H(X, T) \rangle$ as a function of both the dimensionless position X and time T , as obtained from numerical solutions of the dimensionless version (see text) of Eq. (1), with $N = 5$, and for $h_i/\epsilon = 10$ (left) or $h_i/\epsilon = 0.2$ (right). The thick solid lines indicate $\langle H(X, T) \rangle = 0.03$ as an arbitrary reference.

noise over a space interval x and a time interval t . By assuming that the average area conservation in the (x, z) -plan can be expressed as $\langle h_0(t) \rangle \langle R(t) \rangle \sim h_i R_i$, we get

$$\frac{\langle h_0(t) \rangle}{\epsilon} \left[1 + \frac{\langle h_0(t) \rangle}{\epsilon} \right]^3 \sim \frac{\tau_\Gamma}{t} \quad (4)$$

where $\tau_\Gamma = 6\mu h_i^3 R_i^3 b / (k_B T_A \epsilon^4)$ is the characteristic time scale for the stochastic leveling dynamics. Interestingly, Eq. (4) describes a complete crossover between two asymptotic regimes in the stochastic leveling dynamics – a situation that is reminiscent of the bending case but with different exponents and time scale: for $\langle h_0(t) \rangle / \epsilon \gg 1$, we obtain $\langle h_0(t) \rangle / \epsilon \sim (\tau_\Gamma / t)^{1/4}$, and thus we recover $\langle h_0(t) \rangle \sim t^{-1/4}$ [24]; while for $\langle h_0(t) \rangle / \epsilon \ll 1$, we get $\langle h_0(t) \rangle / \epsilon \sim \tau_\Gamma / t$. We expect the crossover between the two asymptotic regimes to occur around $\langle h_0(t) \rangle / \epsilon \approx 1$, *i.e.* around $t/\tau \approx 1/8$.

In order to test the prediction in Eq. (4), we compute the numerical solution of the dimensionless version of Eq. (1) for $5 \leq N \leq 8$, with $h_i/\epsilon \in [10^{-1}, 10^2]$. By averaging over a minimum of 30 realizations, we study specifically $\langle h_0(t) \rangle / \epsilon$ as a function of t/τ_Γ and the results are plotted in Fig. 6. The data from the numerical solutions is in good agreement with Eq. (4) for all $\langle h_0(t) \rangle / \epsilon$, with no adjustable parameter. Our results highlight that Eq. (4) gives an accurate prediction for the stochastic leveling dynamics and show that the missing pre-factor is close to unity. Finally, in order to highlight further the underlying self-similarity associated with each of the two asymptotic regimes, the insets of Fig. 6 show the corresponding full bump height profiles rescaled according to Eq. (4). In each asymptotic regime the height profiles collapse onto a universal shape and confirm the overall self-similarity in the dynamics.

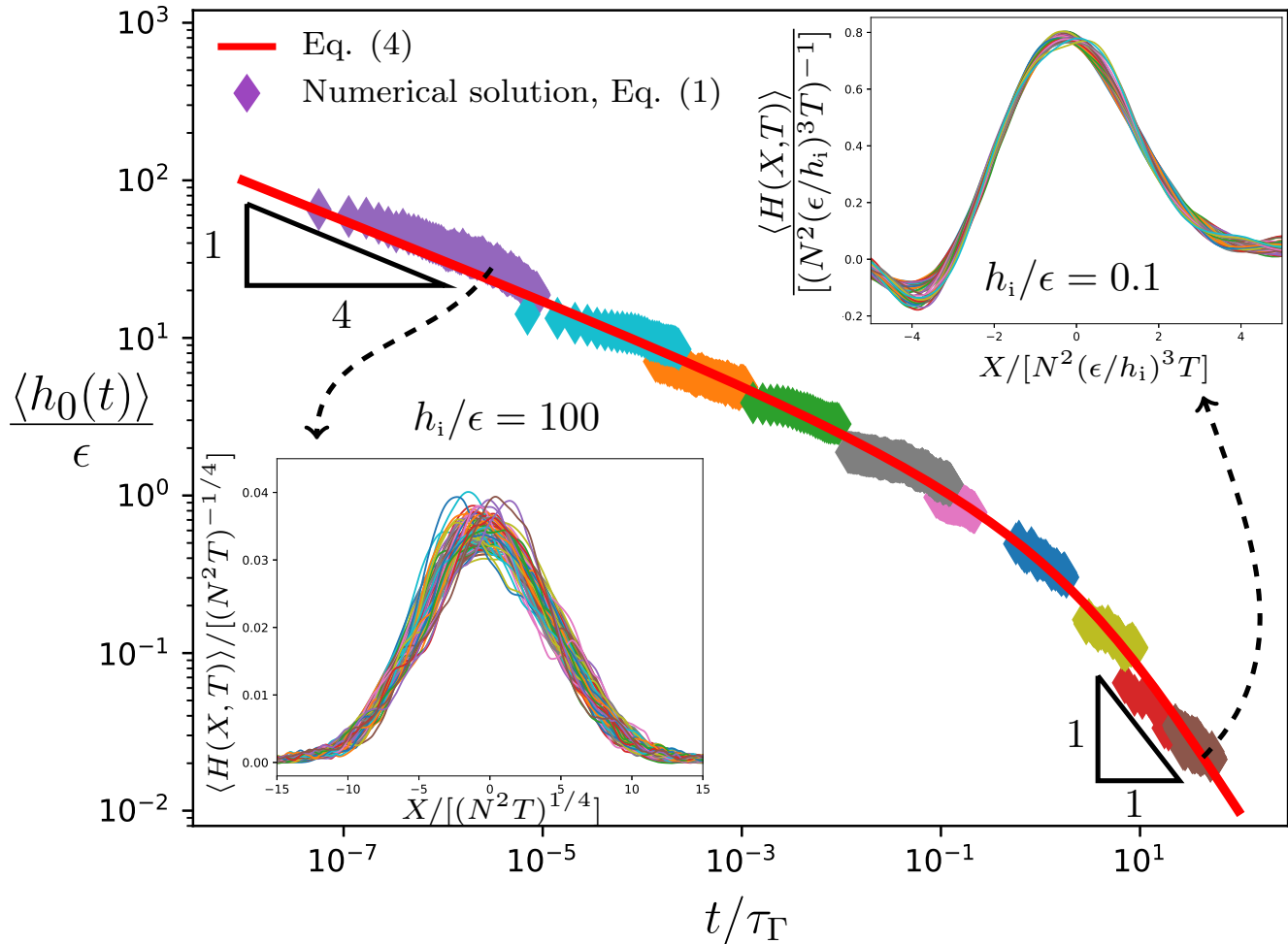


FIG. 6. Non-dimensional bump height as a function of dimensionless time in the stochastic leveling dynamics, for different initial values of $h_i/\epsilon \in [10^{-1}, 10^2]$. The coloured diamond-shaped markers are rescaled data points from the numerical solutions of Eq. (1) with $5 \leq N \leq 8$. Each data set is an average from minimum 30 numerical solutions. The solid red line corresponds to Eq. (4) with unit prefactor. The insets show rescaled bump height profiles for $h_i/\epsilon = 100$ with $T \in [1, 10] \times 10^{-3}$ (lower left); and for $h_i/\epsilon = 0.1$ with $T \in [4, 4.6] \times 10^{-3}$ (upper right).

V. CONCLUSION

We have described the elastohydrodynamic and stochastic leveling of an elastic plate placed atop a thin viscous film. By combining numerical solutions, scaling analysis, and experiments, we identified various canonical regimes. Our results highlighted the importance of the driving mechanism, either by elastic bending of the plate or thermal fluctuations and the influence of the aspect ratio of the bump height to the film height. For each of these two driving mechanisms, a crossover between two distinct asymptotic regimes is controlled by the aspect ratio. These findings can be helpful to explain relaxation processes in elastohydrodynamic settings, which can be found in biological, engineering, or geological processes.

ACKNOWLEDGMENTS

The financial support by the Research Council of Norway (project grant 263056), the Natural Science and Engineering Research Council of Canada and the Joliot Chair of ESPCI Paris is gratefully acknowledged. The authors also thank Tak Shing Chan, Miroslav Kuchta, Corentin Mailliet, René Ledesma-Alonso, Maxence Arutkin, Elie Raphaël, Howard Stone, Pauline Olive, Katelyn Dixon, Paul Fowler, and Mark Ilton, for interesting discussions and preliminary

works in different geometries.

-
- [1] N. J. Balmforth, R. V. Craster, and A. C. Rust. Instability in flow through elastic conduits and volcanic tremor. *Journal of Fluid Mechanics*, 527:353–377, 2005.
- [2] C. Michaut. Dynamics of magmatic intrusions in the upper crust: Theory and applications to laccoliths on earth and the moon. *Journal of Geophysical Research: Solid Earth*, 116(B5), 2011.
- [3] T. V. Ball and J. A. Neufeld. Static and dynamic fluid-driven fracturing of adhered elastica. *Physical Review Fluids*, 3(7):074101, 2018.
- [4] L. E. Bilston, D. F. Fletcher, A. R. Brodbelt, and M. A. Stoodley. Arterial pulsation-driven cerebrospinal fluid flow in the perivascular space: a computational model. *Computer Methods in Biomechanics & Biomedical Engineering*, 6(4):235–241, 2003.
- [5] D. Takagi and N. J. Balmforth. Peristaltic pumping of viscous fluid in an elastic tube. *Journal of Fluid Mechanics*, 672:196–218, 2011.
- [6] R. Borcia, M. Bestehorn, S. Uhlig, M. Gaudet, and H. Schenk. Liquid pumping induced by transverse forced vibrations of an elastic beam: A lubrication approach. *Physical Review Fluids*, 3(8):084202, 2018.
- [7] D. A. Sanchez, Z. Dai, P. Wang, A. Cantu-Chavez, C. J. Brennan, R. Huang, and N. Lu. Mechanics of spontaneously formed nanoblister trapped by transferred 2d crystals. *Proceedings of the National Academy of Sciences*, page 201801551, 2018.
- [8] AE Hosoi and L Mahadevan. Peeling, healing, and bursting in a lubricated elastic sheet. *Physical review letters*, 93(13):137802, 2004.
- [9] R. Huang and Z. Suo. Wrinkling of a compressed elastic film on a viscous layer. *Journal of Applied Physics*, 91(3):1135–1142, 2002.
- [10] Hugues Vandeparre, Sylvain Gabriele, Fabian Brau, Cyprien Gay, Kevin Kit Parker, and Pascal Damman. Hierarchical wrinkling patterns. *Soft Matter*, 6:5751–5756, 2010.
- [11] T. T. Al-Housseiny, I. C. Christov, and H. A. Stone. Two-phase fluid displacement and interfacial instabilities under elastic membranes. *Physical review letters*, 111(3):034502, 2013.
- [12] I. J. Hewitt, N. J. Balmforth, and J. R. De Bruyn. Elastic-plated gravity currents. *European Journal of Applied Mathematics*, 26(1):1–31, 2015.
- [13] Arie Tulchinsky and Amir D Gat. Transient dynamics of an elastic hele-shaw cell due to external forces with application to impact mitigation. *Journal of Fluid Mechanics*, 800:517–530, 2016.
- [14] S. B. Elbaz and A. D. Gat. Axial creeping flow in the gap between a rigid cylinder and a concentric elastic tube. *Journal of Fluid Mechanics*, 806:580–602, 2016.
- [15] A. Carlson and L. Mahadevan. Similarity and singularity in adhesive elastohydrodynamic touchdown. *Physics of Fluids*, 28(1):011702, 2016.
- [16] M. Arutkin, R. Ledesma-Alonso, T. Salez, and E. Raphaël. Elastohydrodynamic wake and wave resistance. *Journal of fluid mechanics*, 829:538–550, 2017.
- [17] Ousmane Kodio, Ian M. Griffiths, and Dominic Vella. Lubricated wrinkles: Imposed constraints affect the dynamics of wrinkle coarsening. *Phys. Rev. Fluids*, 2:014202, Jan 2017.
- [18] A. Juel, D. Pihler-Puzović, and M. Heil. Instabilities in blistering. *Annual Review of Fluid Mechanics*, 50:691–714, 2018.
- [19] J. R. Lister, G. G. Peng, and J. A. Neufeld. Viscous control of peeling an elastic sheet by bending and pulling. *Physical review letters*, 111(15):154501, 2013.
- [20] L. H. Tanner. The spreading of silicone oil drops on horizontal surfaces. *Journal of Physics D: Applied Physics*, 12(9):1473, 1979.
- [21] P. G. De Gennes. Wetting: statics and dynamics. *Reviews of modern physics*, 57(3):827, 1985.
- [22] S. L. Cormier, J. D. McGraw, T. Salez, E. Raphaël, and K. Dalnoki-Veress. Beyond tanner’s law: Crossover between spreading regimes of a viscous droplet on an identical film. *Physical review letters*, 109(15):154501, 2012.
- [23] N. Bergemann, A. Juel, and M. Heil. Viscous drops on a layer of the same fluid: from sinking, wedging and spreading to their long-time evolution. *Journal of Fluid Mechanics*, 843:1–28, 2018.
- [24] B. Davidovitch, E. Moro, and H. A. Stone. Spreading of viscous fluid drops on a solid substrate assisted by thermal fluctuations. *Physical review letters*, 95(24):244505, 2005.
- [25] Vincent Démery and David S. Dean. Perturbative path-integral study of active- and passive-tracer diffusion in fluctuating fields. *Phys. Rev. E*, 84:011148, Jul 2011.
- [26] S Nestic, R Cuerno, E Moro, and L Kondic. Fully nonlinear dynamics of stochastic thin-film dewetting. *Physical Review E*, 92(6):061002, 2015.
- [27] A. Carlson. Fluctuation assisted spreading of a fluid filled elastic blister. *Journal of Fluid Mechanics*, 846:1076–1087, 2018.
- [28] S. Marbach, D. S. Dean, and L. Bocquet. Transport and dispersion across wiggling nanopores. *Nature Physics*, page 1, 2018.
- [29] G. K. Batchelor. *An introduction to fluid dynamics*. Cambridge university press, 2000.
- [30] L. D. Landau and E. M. Lifshitz. *Course of Theoretical Physics Vol 7: Theory and Elasticity*. Pergamon Press, 1959.

- [31] G. Grün, K. Mecke, and M. Rauscher. Thin-film flow influenced by thermal noise. *Journal of Statistical Physics*, 122(6):1261–1291, 2006.
- [32] A. Logg, K.A. Mardal, and G. Wells. *Automated solution of differential equations by the finite element method: The FEniCS book*, volume 84. Springer Science & Business Media, 2012.
- [33] T. Oliphant. NumPy: A guide to NumPy. USA: Trelgol Publishing, 2006-. [Online; accessed 12/20/18].
- [34] Rafael D. Schulman, John F. Niven, Michiel A. Hack, Christian DiMaria, and Kari Dalnoki-Veress. Liquid dewetting under a thin elastic film. *Soft Matter*, 14(18):3557–3562, 2018.
- [35] Joshua D. McGraw, Thomas Salez, Oliver Bäümchen, Elie Raphaël, and Kari Dalnoki-Veress. Self-similarity and energy dissipation in stepped polymer films. *Physical Review Letters*, 109(12):128303, 2012.
- [36] Mark Ilton, Miles M.P. Couchman, Cedric Gerbelot, Michael Benzaquen, Paul D. Fowler, Howard A. Stone, Elie Raphaël, Kari Dalnoki-Veress, and Thomas Salez. Capillary leveling of freestanding liquid nanofilms. *Physical Review Letters*, 117(16):167801, 2016.
- [37] Werner Martienssen and Hans Warlimont, editors. *Springer Handbook of Condensed Matter and Materials Data*. Springer, 2005.
- [38] M. Benzaquen, P. Fowler, L. Jubin, T. Salez, K. Dalnoki-Veress, and E. Raphaël. Approach to universal self-similar attractor for the levelling of thin liquid films. *Soft Matter*, 10:8608, 2014.